Available online at www.sciencedirect.com
ScienceDirect
Journal of Computational Physics 225 (2007) 1632–1652
JOURNAL OF COMPUTATIONAL PHYSICS
www.elsevier.com/locate/jcp

The streamline subgrid integration method: I. Quasi-monotonic second-order transport schemes

Kao-San Yeh *

University of Maryland, Baltimore County, MD 21250, United States

Received 17 February 2004; received in revised form 21 August 2006; accepted 12 February 2007
Available online 19 March 2007

Abstract

A new finite-volume method has been developed for conservative and monotonic transport in multiple dimensions without any sort of dimension splitting to emphasize the space–time integrity of the fluid system. The streamline subgrid integration (SSI) method is a combination of the semi-Lagrangian and the finite-volume methods with generalized multidimensional subgrid distributions. Second-order transport schemes are constructed in two dimensions, and their extensions to three dimensions are also discussed. Spurious divergence is rigorously controlled with Lagrangian control volumes, monotonicity is well preserved for both compressible and incompressible flows, and positive-definiteness is always guaranteed. The accuracy and the numerical properties of these schemes are evaluated with both continuous and discontinuous solutions in flows of rigid motion and incompressible deformation where analytic solutions are available. Icosahedral geodesic grids are selected to demonstrate the general nature of the SSI method in spherical geometry that the numerical solutions are virtually not affected by the irregularity of grid structure. We have found that the numerical solutions converge quickly to the analytic solutions, and the SSI second-order schemes are relatively more beneficial for high-resolution applications.

Keywords: Conservative; Monotonic; Positive-definite; Semi-Lagrangian; Finite-volume; Transport; Multidimensional; Icosahedral; Geodesic

1. Introduction

The development of finite-volume methods for solving fluid-dynamics problems with computers can be traced back to the original work of Courant et al. [1] as early as in 1952, where the conservation and monotonicity properties for non-divergent transport in one dimension are automatically guaranteed by linear interpolation following the characteristics of invariants. Godunov [2] emphasized the importance of monotonicity for discontinuous solutions in 1959 that "The use of schemes which do not have this property is not

* Present address: Code 613, NASA Goddard Space Flight Center, Greenbelt, MD 20771, United States. Tel.: +1 3016146238; fax: +1 3016146297.
E-mail address: kYeh@postit.gsfc.nasa.gov

0021-9991/$ - see front matter
doi:10.1016/j.jcp.2007.02.033

sensible, since the effect of non-monotonicity manifests itself precisely in sharply varying solutions, such as shock waves.'' By requiring the monotonicity condition, Godunov proved that the characteristic method of Courant et al. was the ''best'' transport scheme for discontinuous solutions in the sense that the underlying subgrid distributions would remain monotonic if the material under transport were monotonic at the initial time.

Following Godunov's methodology [2], van Leer [3] generalized the first-order, piecewise constant subgrid distributions to the piecewise linear ones for second-order accuracy, and the accuracy was further improved by Colella and Woodward [4] with piecewise parabolic subgrid distributions. We refer to this type of approach as the *geometric finite-volume methods*, in the sense that the subgrid distributions of the material under transport are explicitly defined for calculating the transport fluxes geometrically. Such a geometric approach provides a rigorous mechanism for localizing the error of numerical transport; it can be particularly useful for long-term applications, such as climate simulations, because widely spread errors could otherwise accumulate to produce unrealistic bias if these errors were not dissipated appropriately. In addition to Godunov's emphases on monotonicity for discontinuous solutions, we believe that monotonicity is also important for retaining the reality of continuous solutions, such as the characteristic wave lengths of mass distribution, and thereby contributing to the convergence of numerical solutions.

Geometric finite-volume methods are often extended to multiple dimensions by integrating subgrid distributions over the domain of dependence implied by the characteristics. Accurate and efficient multidimensional transport has been achieved by combining one-dimensional (1D) subgrid distributions [2–4] with modifications that account for multidimensional effects, *e.g.* the corner contribution of Colella [5], and the cross adjustment of Lin and Rood [6]. Such modifications, however, are not sufficient to fully control the oscillations, and the use of 1D subgrid distributions can affect the maintenance of monotonicity and the localization of conservation in multiple dimensions. Following van Leer's proposal [7], Bell et al. [8] extended Colella's method [5] for transport in porous media with more general consideration of characteristics and bilinear subgrid distributions. These works are closely related to the method proposed in this article.

As modern computers are emphasizing distributed memory, the efficiency of parallel computation with explicit domain decomposition has become an essential issue for many types of application. For instance, the parallel efficiency of most global atmosphere models is still limited by 1D domain decomposition, because of the use of the traditional longitude–latitude grids where the meridians converge at the poles. Although the longitude–latitude grids are perfectly orthogonal, and hence convenient for using 1D subgrid distributions, the pole problem imposes a significant overhead for implementing explicit two-dimensional (2D) domain decomposition. To fundamentally resolve the issue of parallel efficiency in spherical geometry, it appears desirable to use quasi-uniform yet non-orthogonal grids, such as the (icosahedral) geodesic grids, where there are no computational poles.

Prior to the capability of performing massively parallel computation, Williamson [9] and Sadourny et al. [10] demonstrated the advantage of using geodesic grids that the isotropically quasi-uniform resolution can contribute to the accuracy of modeling large-scale atmospheric motions when the computers became powerful enough to model the atmosphere globally in 1960s. Recent studies on atmospheric modeling with geodesic grids include Heikes and Randall [11] and Tomita et al. [12] for reducing grid-related truncation errors, and Randall et al. [13] have successfully constructed a climate model on this type of grid with excellent parallel efficiency. Furthermore, Harten et al. [14] have developed high-order essentially non-oscillatory schemes that allow variable resolution, these schemes may also be useful for modeling with geodesic grids.

We propose to extend the geometric finite-volume methods with multidimensional subgrid distributions, focusing on the accurate application of non-orthogonal grids for efficient parallel computation in spherical geometry. We emphasize tracing the invariants in the discrete grid space with Lagrangian control volumes, which are specified by approximate streamlines with the semi-Lagrangian method of Robert [15] – see also Staniforth and Côté [16] for a review on the semi-Lagrangian methods. The proposed streamline subgrid integration (SSI) method is thus a combination of the semi-Lagrangian and the geometric finite-volume methods, and our first step is to generalize van Leer's second-order transport schemes [3] to multiple dimensions. To demonstrate the general nature of the SSI method, we have selected the geodesic grid (Fig. 1) designed by Tomita et al. [12], where mass centers and spring dynamics are used to reduce grid-related truncation errors. The accuracy and the numerical properties of the SSI second-order transport schemes are evaluated with both

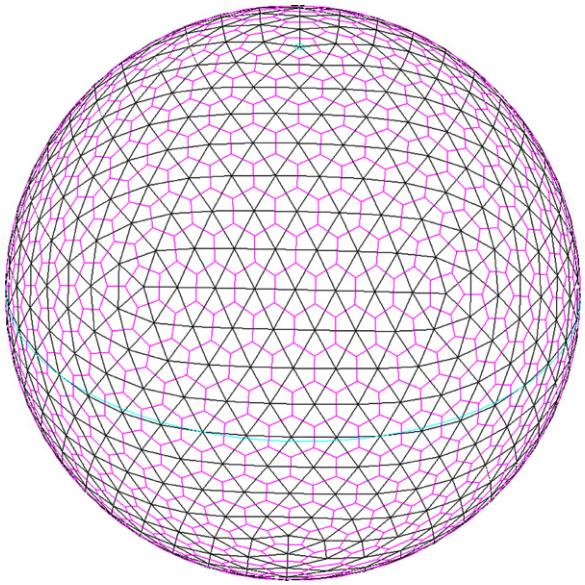

Fig. 1. Spring-dynamics icosahedral geodesic grid with mass centers. The grid cells are depicted with magenta lines, the mass centers of the grid cells are connected with black lines, the equator is indicated by the cyan curve, and the north pole is located at the center of the cyan circle. (For interpretation of the references to colour in this figure legend, the reader is referred to the web version of this article.)

continuous and discontinuous solutions in incompressible flows where analytic solutions are available. In addition to the solid-body rotation test proposed by Williamson et al. [17], we have extended it to a simple incompressible deformational flow to better investigate the numerical properties, such as spurious divergence, monotonicity and positive-definiteness.

2. The streamline subgrid integration method

To construct approximate solutions to the mass conservation law with prescribed velocity, we partition the fluid continuum into a set of fluid elements, and trace them upstream with Lagrangian control volumes (Fig. 2). Let $\overrightarrow{V}$ be the prescribed velocity, ρ the mass density and t is the time coordinate, the mass conservation law can be written as

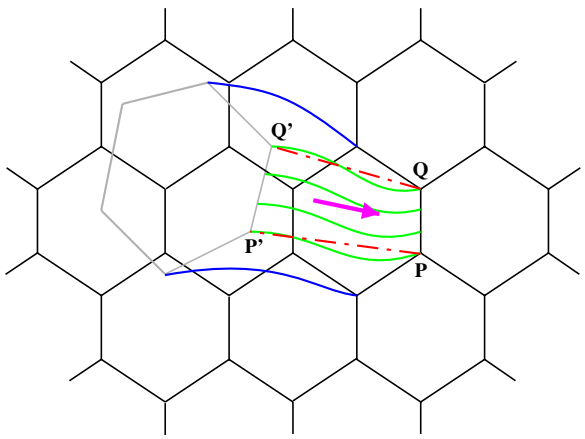

Fig. 2. A Lagrangian control volume under transport in the time interval $[t_0, t_1]$. The Lagrangian control volume at the initial time t_0 is enclosed by the gray lines, it coincides with a grid cell (black lines) downstream at a subsequent time t_1, with the particles initially at P' and Q' arriving at P and Q, respectively.

$$\frac{\partial \rho}{\partial t} + \nabla \cdot (\rho \overrightarrow{V}) = 0. \tag{1}$$

Given a set of mean values $\{\bar{\rho}_i\}$ of mass density for the fluid elements contained in the grid cells at the initial time t_0, we seek for a new set of cell-mean density $\{\tilde{\rho}_i\}$ at a subsequent time $t_1 = t_0 + \Delta t$, as an approximate solution after a short time of transport. The approximate solution for a longer time is obtained with a sequence of such small time steps. Integrating Eq. (1) from t_0 to t_1 over the ith cell Ω_i, we obtain by Gauss divergence theorem that

$$(\tilde{\rho}_i - \bar{\rho}_i) + \frac{1}{A_i} \int_{t_0}^{t_1} \oint_{\partial \Omega_i} (\rho \overrightarrow{V} \cdot \widehat{n}) \mathrm{d}l \, \mathrm{d}t = 0, \tag{2}$$

where A_i denotes the area of Ω_i, $\mathrm{d}l$ the length of an infinitesimal segment of the contour $\partial\Omega_i$ enclosing Ω_i and $\widehat{n}$ is the unit vector normal to the contour segment, pointing outward of Ω_i. Note that the differential $(\rho \overrightarrow{V} \cdot \widehat{n}) \mathrm{d}l \, \mathrm{d}t$ refers to the mass flux crossing an infinitesimal contour segment in an instant time, and the issue is down to the determination of the total mass fluxes crossing the cell edges during the time interval $[t_0, t_1]$.

We first observe that each fluid particle has a constant Lagrangian coordinate following its own trajectory, as illustrated with the green curves in Fig. 2. If the velocity is independent of time, the trajectories coincide with the streamlines at any time, and the material is confined by the streamlines during the transport. Thus for a time-independent velocity field, the material that flows over a cell edge is just the material present in the *upstream area* swept by the corresponding edge of the Lagrangian control volume (Fig. 2), and the mass flux crossing a cell edge within $[t_0, t_1]$ is exactly the mass originally contained in the upstream area at t_0. It remains to determine a set of streamlines that represent $[t_0, t_1]$, and to construct detailed subgrid distributions ρ from the cell-mean values $\{\bar{\rho}_i\}$, so that the mass flux can be estimated by integrating ρ over an approximate upstream area (dashed red lines in Fig. 2[1]).

Let S_{ij} be the upstream area of the jth edge Γ_{ij} of Ω_i, $\widehat{\mu}_{ij}$ the unit normal of Γ_{ij} pointing outward of S_{ij}, $\widehat{n}_{ij}$ the unit normal of Γ_{ij} pointing outward of Ω_i and m_i is the total number of edges of Ω_i. We define the flux vector $\overrightarrow{F}_{ij}$ and approximate Eq. (2) as

$$(\tilde{\rho}_i - \bar{\rho}_i) + \frac{1}{A_i} \sum_{j=1}^{m_i} \overrightarrow{F}_{ij} \cdot \widehat{n}_{ij} = 0, \quad \overrightarrow{F}_{ij} = \left(\int_{S_{ij}} \rho \, \mathrm{d}S \right) \widehat{\mu}_{ij}. \tag{3}$$

This formulation is exact for steady flows if analytic streamlines are used to specify the upstream areas, and if analytic subgrid distributions are used to evaluate the *upstream integral* in Eq. (3). The SSI algorithm thus consists of three major steps:

(1) Determine the upstream areas S_{ij} with approximate streamlines (Section 3).
(2) Determine the subgrid distributions ρ with the cell-mean values $\{\bar{\rho}_i\}$ (Section 4).
(3) Integrate the subgrid distributions ρ over the upstream areas S_{ij} (Section 5).

To simplify the algorithm, we approximate the upstream area of a cell edge with a spherical quadrangle consisting of the cell edge, the two approximate trajectories arriving at the endpoints of the cell edge, and the *upstream edge* that connects the two departure points. Fig. 3 illustrates the nature of invariant of the SSI algorithm. The material in an upstream area on the left of a cell edge (solid green lines) flows to the right and yields a positive flux (outflow), and an upstream area on the right of a cell edge (dashed green lines) yields a negative flux (inflow). The material in an overlapped upstream area flows into the grid cell from one edge and flows out from another, resulting in the cancellation of mass fluxes in Eq. (3), and the net flux is the sum of a positive area integral (red arrows) over the grid cell (black lines) and a negative one (purple arrows) over the Lagrangian control volume at the initial time (gray lines). This implies that the mass contained in the Lagrangian control volume at the initial time is equal to the mass contained in the grid cell after transport.

[1] For interpretation of the references to colour in the text, the reader is referred to the web version of this article.

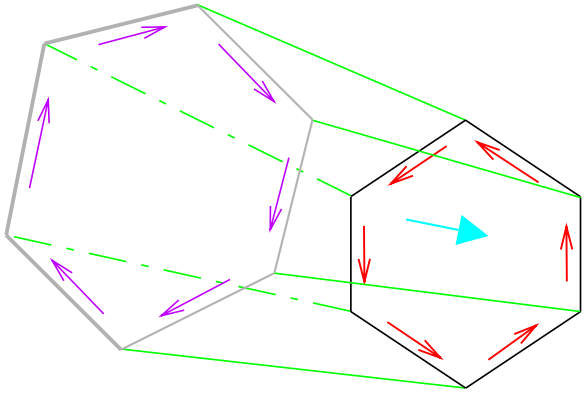

Fig. 3. The nature of invariant of the SSI algorithm. The material contained in the Lagrangian control volume (gray lines) is transported to the grid cell (black lines). See text for details.

Unlike traditional semi-Lagrangian methods that use an approximate trajectory arriving at a cell center as the characteristic of an invariant, the SSI method defines a characteristic collectively with all the approximate trajectories of the particles contained in a Lagrangian control volume. Based on the advection equation for incompressible flows,

$$\frac{\mathrm{d}\rho}{\mathrm{d}t} = \frac{\partial\rho}{\partial t} + \vec{V}\cdot\nabla\rho = 0, \tag{4}$$

traditional semi-Lagrangian methods determine the value of ρ at a cell center by interpolation to an upstream point; the divergence term $\rho\nabla\cdot\vec{V}$ is then supplemented to complete the estimation of ρ for compressible flows. While the traditional semi-Lagrangian procedure offers a very efficient and quite accurate solution to the advection problem, it may not be ideal for solving the mass conservation law, because the pointwise determined values cannot precisely represent the Lagrangian control volumes that define the invariants for the mass conservation law in the discrete space, and spurious divergence may occur to contaminate the numerical solution – see Section 3 for more discussion on spurious divergence. In the sense of characteristics, the proposed SSI method can be considered as a generalization of the traditional semi-Lagrangian methods from the finite-difference to the finite-volume formulation with the inclusion of the divergence term in the invariants.

3. Integration areas and spurious divergence

The first step of the SSI algorithm is to specify an approximate upstream area for each cell edge with the *upstream positions* of the cell corners, i.e., the departure points of the particles arriving at the cell corners. We determine these upstream positions with the velocity $\vec{V}^*$ given at the middle time $t^* = t_0 + \Delta t/2$, so that the trajectories can be approximated in a sense of time averaging [15]. We assume that the values of $\vec{V}^*$ are given at both cell centers and corners – if $\vec{V}^*$ is given at the cell centers only, we interpolate it to the cell corners. Following Côté [18], we use 3D Cartesian coordinates with the origin O at the center of the unit sphere, and constrain the motion of the fluid to the spherical surface.

To determine the upstream position X of a cell corner P_1, we first guess X as if the particle were moving from X to P_1 along the geodesic line $\overline{XP_1}$ with $\vec{U}^* = \vec{V}^*(P_1)$:

$$\overrightarrow{OX} = \frac{\overrightarrow{OY}}{|\overrightarrow{OY}|}, \quad \overrightarrow{OY} = \overrightarrow{OP}_1 - \vec{U}^*\Delta t. \tag{5}$$

Next, we estimate the velocity at the first-guessed X by linear interpolation from the cell centers and corners, as illustrated in Fig. 4. We divide the cell containing X into spherical triangles with the radii from its center to corners. Suppose X falls in the spherical triangle $\Delta P_1P_2P_3$, where P_2 is a corner next to P_1, and P_3 is the cell center. Let s, s_1, s_2, s_3 be the areas of the spherical triangles $\Delta P_1P_2P_3$, ΔXP_2P_3, ΔXP_3P_1, ΔXP_1P_2, respectively, we obtain

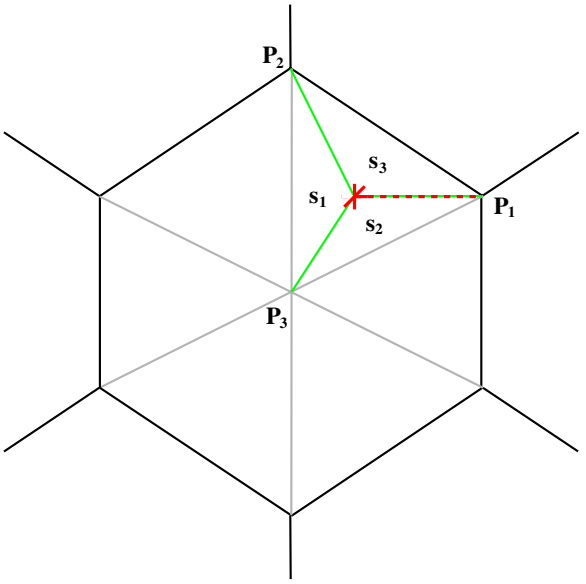

Fig. 4. Linear interpolation of velocity to the upstream position (red X) of the cell corner P_1. Values of velocity are given at the cell center P_3 and the cell corners P_1 and P_2. The interpolation weights at P_1, P_2 and P_3 are proportional to the areas of the sub-triangles s_1, s_2 and s_3, respectively. (For interpretation of the references to colour in this figure legend, the reader is referred to the web version of this article.)

$$\overrightarrow{U} = \frac{1}{s}\{s_1 \overrightarrow{V}^*(P_1) + s_2 \overrightarrow{V}^*(P_2) + s_3 \overrightarrow{V}^*(P_3)\}. \tag{6}$$

The interpolated velocity, however, is not tangent to the spherical surface in general, and we constrain it to the spherical surface by subtracting its normal component:

$$\overrightarrow{V}^*(X) = \overrightarrow{U} - (\overrightarrow{U} \cdot \overrightarrow{OX})\overrightarrow{OX}. \tag{7}$$

We proceed to use Eq. (5) for a more accurate upstream position with the average velocity

$$\overrightarrow{U}^* = \frac{1}{2}\{\overrightarrow{V}^*(X) + \overrightarrow{V}^*(P_1)\}. \tag{8}$$

Note that the average velocity estimated by Eq. (8) does not need to be constrained to the spherical surface, because the projection in Eq. (5) will lead to the same solution.

The procedure to estimate the average velocity with Eqs. (6)–(8), and hence the upstream position by Eq. (5), can be applied recursively to improve the accuracy to certain extent. This is the *trajectory iteration* procedure used in traditional semi-Lagrangian methods [16], except that we have reformulated it with geometric elements for geodesic grids.

Pudykiewicz et al. [19] show that the trajectory iteration converges if the velocity field $\overrightarrow{V}^*$ satisfies the *Lipschitz condition* that the time step Δt be smaller than the reciprocal of the maximum absolute value of the wind shear in any coordinate direction. Let Δx be the distance between two neighboring cell centers P and Q, Δu the component of $\Delta\overrightarrow{V}^* = \overrightarrow{V}^*(P) - \overrightarrow{V}^*(Q)$ along $\overline{PQ}$, and Δv the component of $\Delta\overrightarrow{V}^*$ perpendicular to $\overline{PQ}$, the Lipschitz condition for geodesic grids can be expressed with the *Lipschitz number* that

$$L = \max\left(\left|\frac{\Delta u}{\Delta x}\right|, \left|\frac{\Delta v}{\Delta x}\right|\right)\Delta t < 1. \tag{9}$$

Furthermore, Staniforth and Pudykiewicz [20] find that it is sufficient to use linear interpolation to estimate the average velocity for the approximate trajectory, and only *two iterations* are needed to determine the upstream positions with satisfactory accuracy – as we have observed in our formulation for geodesic grids. We have also observed that the trajectories are not well converged with only one iteration, and there is virtually no benefit from the third iteration or more.

Beyond the stability condition, we consider spurious divergence an important factor for solving the mass conservation law, because it can lead to the violation of monotonicity and produce spurious gravity waves to contaminate the solution. The spurious divergence of the SSI method arises from the error in specifying the Lagrangian control volumes. The first source originates from the approximation to the trajectories by the streamlines given at the middle time. With the semi-Lagrangian trajectory iteration, the error in determining the upstream positions of the cell corners is confined within second-order accuracy in time [16]. The second source comes from the linear approximation to the upstream areas of cell edges with spherical quadrangles, the error in specifying the Lagrangian control volumes is thus confined within second-order accuracy in space. We have found the second-order accuracy in both time and space sufficient for controlling the spurious divergence.

Spurious divergence can be partly examined by testing whether an initially uniform distribution would remain uniform in an incompressible flow where there is no true divergence – we refer to this test as the *incompressible condition*. From the nature of invariant (Fig. 3), we see that the SSI method satisfies the incompressible condition for rigid motion if analytic upstream positions are used to define the upstream areas, and if the subgrid distributions ρ in Eq. (3) are uniform with the same value as that of the initial condition $\{\bar{\rho}_i\}$. In Section 4, we construct the subgrid distributions from the initial cell-mean values such that the uniformity of the cell-mean values is inherited by the subgrid distributions. In Section 6, we test the incompressible condition and show that the semi-Lagrangian trajectory iteration does provide sufficient accuracy in the sense that the spurious divergence is negligible for both solid-body rotation and incompressible deformation.

4. Subgrid distributions and monotonicity

The second step of the SSI algorithm is to construct detailed subgrid distributions from the cell-mean values given at the initial time. We generalize van Leer's piecewise linear subgrid distributions [3] from one to two dimensions for arbitrary grids. Instead of using line segments for 1D subgrid distributions, we use local planes to approximate 2D subgrid distributions up to second-order accuracy.

Suppose we wish to determine the subgrid distribution ρ for a cell Ω_0 centered at P_0, which has n neighboring cells $\Omega_1, \ldots, \Omega_n$, centered at $P_1, \ldots, P_n$, respectively (Fig. 5). We first project $P_1, \ldots, P_n$ from the center of the sphere to the plane tangent to the sphere at P_0, and describe the projected points in *local Cartesian coordinates* with the origin defined at P_0, the x-axis in the east, and the y-axis in the north. Given the mean values $\bar{\rho}_0, \ldots, \bar{\rho}_n$ for $\Omega_0, \ldots, \Omega_n$, respectively, we seek for a linear function ρ such that

$$\rho(x, y) = \bar{\rho}_0 + ax + by, \quad c = \sqrt{a^2 + b^2}, \tag{10}$$

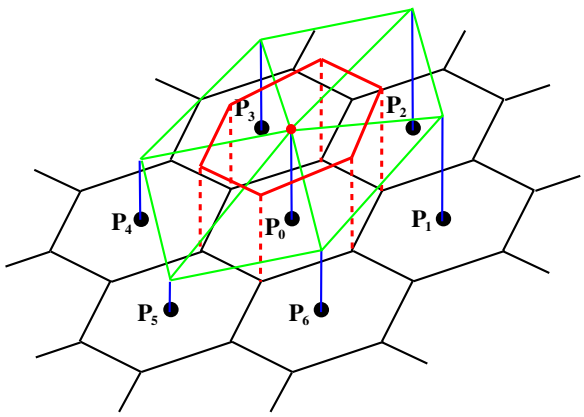

Fig. 5. Second-order subgrid distribution (red hexagon) for the cell centered at P_0. Mean values (blue lines) at cell centers (black spots) are first used to calculate the slopes of the auxiliary planes (green triangles), these slopes are then averaged to determine the slopes of the distribution plane that has the mean value (red spot) at P_0. (For interpretation of the references to colour in this figure legend, the reader is referred to the web version of this article.)

where the slopes a and b are to be determined with $\bar{\rho}_0, \ldots, \bar{\rho}_n$. Note that the mean values are represented at the cell centers with second-order accuracy, as we have defined the cell centers with the mass centers of the cells (Fig. 1). This also ensures the Leibnitz rule that the integral of a subgrid distribution over a cell be equal to the mass contained in the cell, and thereby enhances the localization of conservation during the transport.

Let (x_i, y_i) be the local Cartesian coordinates of P_i, and $\rho'_i = \bar{\rho}_i - \bar{\rho}_0$, for $i = 1, \ldots, n$. We first fit an auxiliary plane,

$$f(x, y) = \bar{\rho}_0 + a_i x + b_i y, \tag{11}$$

$$a_i = \frac{y_i \rho'_j - \rho'_i y_j}{y_i x_j - x_i y_j}, \quad b_i = \frac{\rho'_i x_j - x_i \rho'_j}{y_i x_j - x_i y_j}, \quad c_i = \sqrt{a_i^2 + b_i^2}, \tag{12}$$

for every three neighboring points P_0, P_i, P_j, $j = \mathrm{mod}(i, n) + 1$, such that $f(x_i, y_i) = \bar{\rho}_i$ and $f(x_j, y_j) = \bar{\rho}_j$, then take average of the slopes a_i and b_i to obtain the mean slopes

$$\bar{a} = \frac{1}{n} \sum_{i=1}^{n} a_i, \quad \bar{b} = \frac{1}{n} \sum_{i=1}^{n} b_i, \quad \bar{c} = \sqrt{\bar{a}^2 + \bar{b}^2}. \tag{13}$$

Note that the denominators in Eq. (12) do not vanish, and hence a_i and b_i are well defined, because P_0, P_i, P_j are not common to any geodesic line. Take $a = \bar{a}$ and $b = \bar{b}$ for Eq. (10), we obtain the *basic subgrid distribution*, which is isotropically second-order accurate.

To preserve the monotonicity of the initial condition in the numerical solution, we limit the slopes of the subgrid distributions with the *quasi-monotonic constraint* using $a = b = 0$ in Eq. (10) if $\bar{c} = 0$, and

$$a = \gamma \bar{a}, \quad b = \gamma \bar{b}, \quad \gamma = \min(\bar{c}, \beta \hat{c})/\bar{c}, \quad \hat{c} = \min(c_1, \ldots, c_n), \quad \text{if } \bar{c} > 0, \tag{14}$$

where $\beta \geqslant 0$ is a *monotonicity parameter* to limit the slopes for desired monotonicity. A greater β allows more accurate slopes but preserves less monotonicity with less diffusion. When $\beta = 0$, Eq. (10) reduces to a constant, and the monotonicity is preserved for any flow if exact Lagrangian control volumes are used for transport. When $\beta > 0$, local extrema are not bounded by their initial cell-mean values, but the subgrid mixing during the transport provides strong diffusion to suppress the overshoots. For the best compromise between accuracy and monotonicity, we recommend using $\beta \geqslant 1$ for compressible flows with the Lipschitz number $L < 1/\beta$. This optimal value of β is suggested by the special case of 1D uniform resolution that the monotonicity in a monotonic region is preserved by the quasi-monotonic constraint when $L < 1/\beta$, if the Lagrangian control volumes are exact.

The monotonicity parameter can also be used to maintain global bounds with optimal accuracy. Let $\Delta\xi$ be the maximum radius of Ω_0, we then have ρ bounded by $\widehat{\rho}$ over Ω_0 if $c\Delta\xi \leqslant |\widehat{\rho} - \bar{\rho}_0|$, which can be achieved by the quasi-monotonic constraint with best accuracy when $\beta\hat{c} = |\widehat{\rho} - \bar{\rho}_0|/\Delta\xi$. Multiple global bounds can be maintained simultaneously, and *positive-definiteness* is achieved when $\widehat{\rho} = 0$ is included as a global bound. We may use a specific β for each cell to optimize the accuracy while maintaining the global bounds.

The quasi-monotonic subgrid distributions defined by Eqs. (10)–(14) can be extended to three dimensions easily – all we need is to add vertical terms to Eqs. (10) and (11) and define the slopes in Eq. (12) with 3D Jacobians. The maintenance of monotonicity and global bounds depends also on the spurious divergence associated with the specification of the Lagrangian control volumes, which should be commensurate to with a smaller value of β to ensure the desired bounding. For the geodesic grids, we use the average resolution at the equator (Δx_e) in place of the maximum cell radius for maintaining positive-definiteness. A good variety of quasi-monotonic transport schemes can be designed for specific purposes by manipulating the monotonicity parameter. In Section 6, we demonstrate the accuracy and numerical properties of the *SSI 2.2 transport scheme* that uses the positive-definite quasi-monotonic subgrid distributions with (i) $\beta = 2$ if $\hat{c} \leqslant \varepsilon/2$, (ii) $\beta = 1$ if $\varepsilon/2 < \hat{c} \leqslant \varepsilon$, (iii) $\beta = 0$ if $\varepsilon < \hat{c}$, where $\varepsilon = |\bar{\rho}_0|/\Delta x_e$, and β and $\hat{c}$ are as defined in Eq. (14). The version number "2.2" refers to the second-order accuracy with $\beta = 2$ for maintaining the monotonicity in moderately deformational flows ($L < 1/2$), except when the global bounding is in effect.

5. Subgrid integration for transport fluxes

The third step of the SSI algorithm is to calculate the transport fluxes by integrating the subgrid distributions over the upstream areas, and hence determine the numerical solution. For a geodesic grid, we observe that each cell edge is surrounded by four cells, and each cell corner is shared by three cells. Defining the grid configuration for a cell edge as in Fig. 6a, we illustrate the subgrid integration procedure with the example shown in Fig. 6b.

We first divide the subgrid integration procedure into the 3×3 cases shown in Fig. 7 with the upstream positions (P' and Q') of the endpoints (P and Q) of the central edge ($\overline{PQ}$), according to the grid configuration defined in Fig. 6a. Suppose P' falls in the south cell, and Q' falls in the north cell, then we have the case (33), where $\overline{P'Q'}$ may intersect the cell edges in four distinct ways (subcases) as shown in Fig. 7. The primary cases are determined by comparing the orientations of the approximate streamlines $\overline{PP'}$ and $\overline{QQ'}$ to those of the cell edges, while the subcases are distinguished by the orientation of the upstream edge $\overline{P'Q'}$ relative to P and Q. Let O be the center of the sphere, we identify the subcase in Fig. 6b with P on the right and Q on the left of $\overline{P'Q'}$ when

$$\sigma_S = (\overrightarrow{P'Q'} \times \overrightarrow{PP'}) \cdot \overrightarrow{OP} > 0, \quad \sigma_N = (\overrightarrow{P'Q'} \times \overrightarrow{QQ'}) \cdot \overrightarrow{OQ} < 0. \tag{15}$$

Furthermore, we determine the intersections of two geodesic lines by projecting their cross vectors to the spherical surface, *e.g.*

$$\overrightarrow{OB} = \frac{\overrightarrow{OB'}}{|\overrightarrow{OB'}|}, \quad \overrightarrow{OB'} = (\overrightarrow{OP'} \times \overrightarrow{OQ'}) \times (\overrightarrow{OP} \times \overrightarrow{OQ}). \tag{16}$$

Suppose $\overline{P'Q'}$ intersects the southwest edge at A, the central edge at B, and the northeast edge at C, then the upstream area of $\overline{PQ}$ consists of four spherical triangles: $\Delta APP'$ in the south cell, ΔABP in the west cell, ΔBCQ in the east cell, and $\Delta CQQ'$ in the north cell. Projecting A, B, P to the tangent plane at the west cell center, we obtain the local Cartesian coordinates (x_A, y_A), (x_B, y_B), (x_P, y_P) and the mean value over ΔABP by Eq. (10) as

$$\rho^* = \bar{\rho}_W + \frac{a}{3}(x_A + x_B + x_P) + \frac{b}{3}(y_A + y_B + y_P), \tag{17}$$

where $\bar{\rho}_W$ is the mean value over the west cell given at the initial time. Similarly, we can determine the mean values over the other triangles. Let ρ_1^*, ρ_2^*, ρ_3^*, ρ_4^* be the mean values over $\Delta APP'$, ΔABP, ΔBCQ, $\Delta CQQ'$, respectively, and s_1, s_2, s_3, s_4 the corresponding areas, we obtain the net flux crossing $\overline{PQ}$ for the *west cell* as

$$F = \mathrm{sgn}(\sigma_S) \cdot (\rho_1^* s_1 + \rho_2^* s_2) + \mathrm{sgn}(\sigma_N) \cdot (\rho_3^* s_3 + \rho_4^* s_4), \tag{18}$$

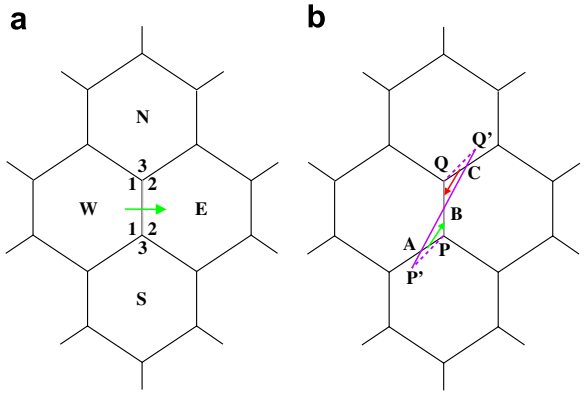

Fig. 6. Determination of transport fluxes by subgrid integration over upstream areas. (a) Configuration of the grid cells around the central edge (gray line) where the fluxes cross. (b) A positive flux (green arrow) from the left of the central edge indicates an outflow, and a negative flux (red arrow) from the right refers to an inflow for the west cell. (For interpretation of the references to colour in this figure legend, the reader is referred to the web version of this article.)

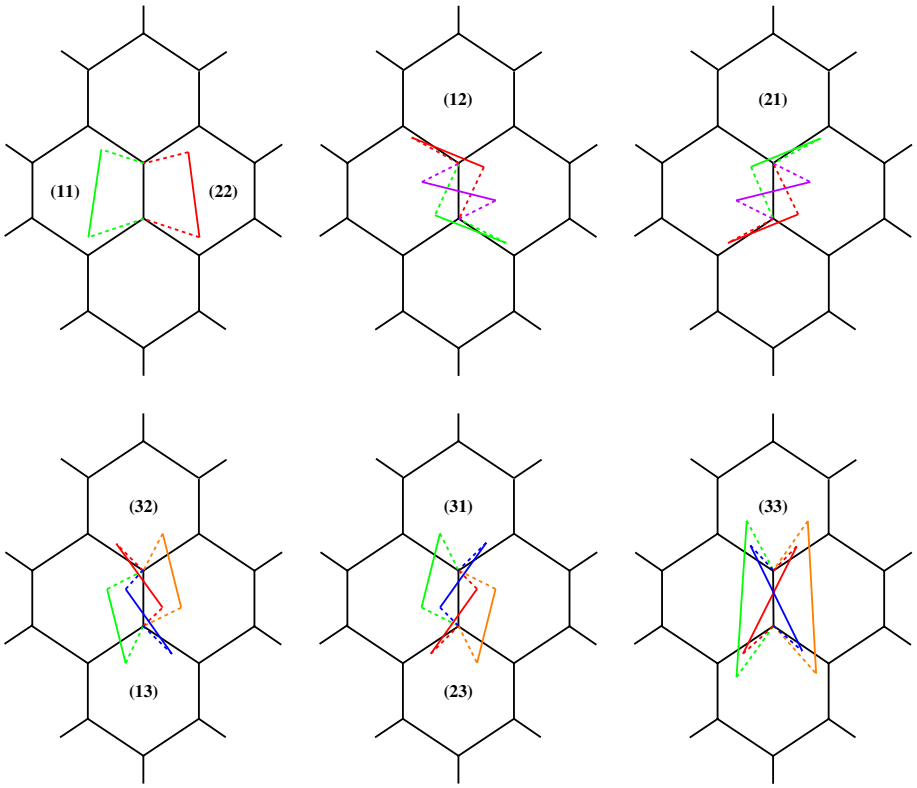

Fig. 7. Subgrid integration cases based on the orientations of approximate streamlines. The first digit of a case number refers to the orientation of the north streamline, and the second digit corresponds to the south streamline, according to the grid configuration defined in Fig. 6a. Except for cases (11) and (22), each case has 2–4 subcases determined by the orientation of the upstream edge relative to the endpoints of the central edge where the fluxes cross.

where we have executed the inner product in Eq. (3) with $F = \overrightarrow{F}_{ij} \cdot \hat{n}_{ij}$. Note that the signs of the fluxes, $\mathrm{sgn}(\sigma_S)$ and $\mathrm{sgn}(\sigma_N)$, are implied by the orientation of $\overline{P'Q'}$ relative to P and Q that the mass originally contained in s_1 and s_2 flows out of the west cell as positive fluxes because these areas are on the left of $\overline{PQ}$, while s_3 and s_4 being on the right of $\overline{PQ}$ yield inflows as negative fluxes to the west cell (Fig. 6b).

In Fig. 7, we have enumerated all possible cases of subgrid integration under the Lipschitz condition that the trajectories do not cross, and the assumption that no fluid particle travels farther than the length of any cell edge within the time step. These cases are sufficient for active transport in a dynamics system where the stability is subject to the fast-moving gravity waves based on the nodes at the cell centers. For more efficient applications with larger time steps, however, we will need to consider more subgrid integration cases. We also note that the SSI algorithm is equivalent to integrating the subgrid distributions over the Lagrangian control volumes directly (Fig. 3). We choose to integrate the upstream areas of the cell edges rather than the Lagrangian control volumes, because the subgrid integration involving all upstream edges of a Lagrangian control volume simultaneously is much more complicated than integrating an upstream area involving only one upstream edge at a time. We outline the algorithm of the SSI second-order transport schemes as follows:

(1) Calculate the upstream positions of the cell corners with Eqs. (5)–(8).
(2) Define the subgrid distribution of mass density for each cell with Eqs. (10)–(14).
(3) Determine the subgrid integration case for each cell edge with Fig. 7.
(4) Calculate the transport fluxes with the subgrid integration, *e.g.* Eqs. (15)–(18).
(5) Calculate the mean mass density after transport with Eq. (3).

6. Numerical experiments

Following Williamson et al. [17], we test the SSI 2.2 transport scheme with solid-body rotation where the axis of rotation is variable with respect to the computational grid. We define the Cartesian coordinate system (x, y, z) with its origin at the center of the sphere, and the spherical coordinate system (λ, θ) with its polar axis coincident with the z-axis, and $\lambda = 0$ in the direction of the x-axis. Rotating these coordinate systems clockwise about the y-axis by an angle α, we obtain the tilted coordinate systems (x', y', z') and (λ', θ'), as shown in Fig. 8. Like the Earth's rotation, the fluid on the spherical surface rotates counterclockwise about the tilted polar axis.

To better investigate the numerical properties, we extend the solid-body rotation test to incompressible deformation by varying the rotation frequency with the latitude. Considering a solid-body rotation about the tilted polar axis with the angular frequency ω_0, we define the angular frequency of the incompressible deformation as

$$\omega(\theta', t) = \omega_0[1 - \sin^2(2\theta')\sin(\omega_0 t)]. \tag{19}$$

Thus we have a rigid motion on each tilted latitude circle – the angular frequency on the tilted equator is constant (ω_0), the angular frequencies on other tilted latitude circles vary with time, but they all have the same period ($2\pi/\omega_0$). The velocity field implied by Eq. (19) is therefore incompressible and purely rotational, while the variation of angular frequency with the latitude (θ') leads to deformation by shearing effect.

Let $\hat{i}, \hat{j}, \hat{k}$ be the unit vectors of the x-, y-, z-axis, respectively, we have the velocity field of the incompressible deformation expressed in Cartesian coordinates as

$$\vec{V} = \omega[-ay\hat{i} + (ax + bz)\hat{j} - by\hat{k}], \tag{20}$$

where $a = \cos(\alpha)$ and $b = \sin(\alpha)$. In terms of the spherical coordinates (λ, θ) with $\hat{\lambda}$ and $\hat{\theta}$ the directional vectors, and R_0 the radius of the sphere, the velocity is expressed as

$$\vec{V} = \omega R_0\{[a\cos(\theta) + b\sin(\theta)\cos(\lambda)]\hat{\lambda} - b\sin(\lambda)\hat{\theta}\}. \tag{21}$$

Given an analytic function $f(\lambda', \theta')$ that defines the initial condition at $t = 0$, we then have the analytic solution at $t = \Delta t$ written as $f(\lambda' - \phi, \theta')$, where

$$\phi = \int_0^{\Delta t} \omega \, dt = \omega_0 \Delta t + \sin^2(2\theta')[\cos(\omega_0 \Delta t) - 1]. \tag{22}$$

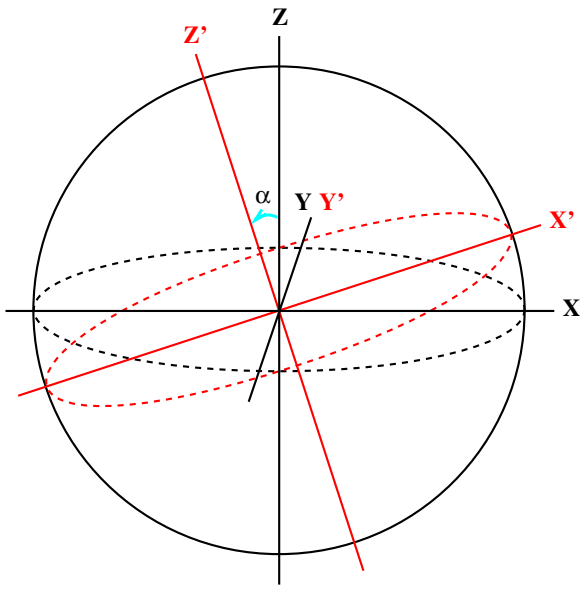

Fig. 8. 3D Cartesian coordinate systems with the origin at the center of the sphere. The z-axis (Z) passes the geographic poles, and the z'-axis (Z') is the axis of rotation.

A geodesic grid consists of ten rhombic regions and two extra grid points for the poles – each region is specified by the centers of the pentagonal cells at the vertices of the rhombus. Suppose each region contains $N \times N$ grid points (cell centers), we then have $(10N^2 + 2)$ grid points for the entire grid, and the equator is covered by $5N$ cells. For the geodesic grid in Fig. 1, we have $N = 8$ with 40 cells covering the equator at the average resolution of approximately 1000 km, it is thus referred to as the *G8 grid*. For simplicity, we use the average resolution on the equator (Δx_e) to represent a geodesic grid, keeping in mind that it is slightly coarser than the average resolution of the entire grid, *e.g.* 961 km for the G8 grid. The G16, G32, G64, G128 grids are therefore also referred to with the approximate resolutions $\Delta x_e \doteq 500$, 250, 125, 63 km, respectively. Following Tomita et al. [12], we modify the geodesic grids with mass centers and spring dynamics to reduce grid-related truncation errors. The reduction of truncation errors is mainly due to the truly second-order representation of the data points at the mass centers (Tomita, personal communication), and partly due to the monotonicity of the grid distribution resulted from the spring dynamics. In particular, we have used non-linear spring dynamics with unit grid parameter [12] to maximize the grid uniformity. The largest distance between two grid points is about 25% greater than the smallest one for such a grid as N approaches to infinity, and the resolution is slightly finer near the pentagons than away from the pentagons.

As proposed in [17], we test the scheme with the Courant number approximately 0.5 for one revolution. We limit the time step Δt such that $C = |\vec{V}|_{\max} \Delta t / \Delta x_e \doteq 0.5$, where $|\vec{V}|_{\max}$ is the maximum wind speed. Using the angular frequency $\omega_0 = 2\pi/(12 \text{ days})$, and the average radius $R_0 = 6,371,220$ m for the Earth, we have $|\vec{V}|_{\max} = \omega_0 R_0 \doteq 38.6$ m/s for the solid-body rotation tests (a1, b1, c1), where we use $\Delta t = 216$, 108, 54, 27, 13.5 min for the G8, G16, G32, G64, G128 grid, respectively. While for the incompressible deformation tests (a2, b2, c2), we have $|\vec{V}|_{\max} \doteq 59.6$ m/s occurred at $\theta' \doteq 35^\circ$ when $\omega_0 t = 3\pi/2$, so we use $\Delta t = 144$, 72, 36, 18, 9 min for the G8, G16, G32, G64, G128 grid, respectively.

Note that the Lipschitz number is a measure of both shearing and compressing effects, while the shearing effect does not necessarily lead to deformation. For the solid-body rotation on the G8 grid with $\Delta t = 216$ min, we actually have the maximum Lipschitz number $L_{\max} \doteq 0.08$ occurred at the poles of rotation, which is purely due to the variation of rotation curvature. While for the incompressible deformation on the G8 grid with $\Delta t = 144$ min, we have $L_{\max} \doteq 0.12$ at $\theta' \doteq 60^\circ$ when $\omega_0 t = 3\pi/2$, which is due to both curvature and frequency variation. Since the incompressible deformation results from the frequency variation, we have the maximum deformation occurred at $\theta' = 22.5^\circ$ with $L \doteq 0.11$ when $\omega_0\, t = 0$, where the contribution of the curvature variation to the Lipschitz number is an order smaller than that of the frequency variation. We also note that the Lipschitz number depends on the time step but not the resolution, and fixing the Courant number leads to the decreasing of the Lipschitz number with increasing resolution. For instance, $L_{\max} \doteq 0.06$ for the incompressible deformation on the G16 grid with $\Delta t = 72$ min.

For all numerical experiments presented in this article, we define the initial conditions at the cell centers pointwise, and these pointwise values are taken as the mean values over the corresponding cells to start the time integration. All velocity fields are prescribed at both the cell centers and corners at the middle of the time steps, and two trajectory iterations are used to determine the upstream positions of the cell corners, unless otherwise mentioned. We measure the accuracy of numerical solutions with the normalized errors:

$$\ell_1 = \frac{\sum |f_i - g_i| A_i}{\sum |f_i| A_i}, \quad \ell_2 = \frac{\sqrt{\sum |f_i - g_i|^2 A_i}}{\sqrt{\sum |f_i|^2 A_i}}, \quad \ell_\infty = \frac{\max(|f_i - g_i|)}{\max(|f_i|)}, \tag{23}$$

where the summation and the maximum functions are evaluated over all grid cells, f_i is the analytic solution, g_i the numerical solution, and A_i the area of the ith grid cell.

6.1. Spurious divergence of solid-body rotation

With the solid-body rotation of a constant field ($\bar{\rho}_i = 1$), we test the incompressible condition to examine the spurious divergence of the SSI method. Because of the isotropic property of geodesic grids, the results are

similar for different rotation angles, and we choose $\alpha = 0$ to better illustrate the influence of the grid structure for this test.

Table 1 summarizes the errors after one revolution, which are purely due to the spurious divergence associated with the specification of the Lagrangian control volumes. Significant error is accumulated if the trajectories are not iterated to achieve second-order accuracy in time, even though the time steps are small with the Courant number only 0.5 and the Lipschitz number only 0.08 on the G8 grid. The error accumulation is a consequence of the persistent spurious convergence toward the poles due to the use of tangential velocity. The spurious divergence is, however, virtually eliminated when the trajectories are iterated for only two times, as illustrated in Fig. 9. This shows the importance of the accuracy in determining the upstream positions. We also note that the errors due to spurious divergence decrease rapidly with increasing resolution, and they are negligible compared to those shown in Tables 3 and 7 where the initial conditions are not uniform.

6.2. Spurious divergence of incompressible deformation

To further investigate the spurious divergence of the SSI method, we test the incompressible condition with the incompressible deformation flow. In addition to the error in upstream positions, Lagrangian control volumes are now twisted, and the linear approximation to the Lagrangian control volumes adds to the error in

Table 1
Statistics of solid-body rotation of a constant field with $\alpha = 0$ after one revolution, using different resolutions and different numbers of trajectory iteration

Grid	Iterations	Minimum	Maximum	ℓ_1 Error	ℓ_2 Error	ℓ_∞ Error
G8	0	0.78559231	1.62948071	0.18633413	0.22663439	0.62948071
G8	2	0.99964556	1.00014065	0.00008760	0.00010708	0.00035444
G16	2	0.99995537	1.00002019	0.00001226	0.00001466	0.00004463
G32	2	0.99999428	1.00000419	0.00000161	0.00000190	0.00000572
G64	2	0.99999892	1.00000105	0.00000020	0.00000024	0.00000108
G128	2	0.99999925	1.00000026	0.00000003	0.00000003	0.00000075

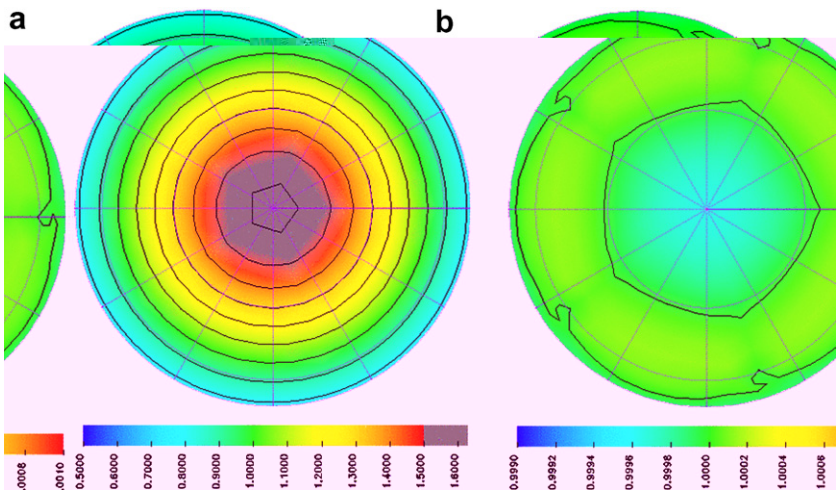

Fig. 9. Solid-body rotation of a constant field with $\alpha = 0$ after one revolution on G8 grid ($\Delta x_e \doteq 1000$ km), using 0 and 2 trajectory iterations in (a) and (b), respectively. The analytic solution has the constant value 1, and the numerical solutions are depicted with both colors and black contours from 0.8 to 1.6 by 0.1. (For interpretation of the references to colour in this figure legend, the reader is referred to the web version of this article.)

divergence. Table 2 summarizes the errors for the incompressible deformation of a constant field with unit value after one revolution, which are in general greater than those in Table 1 for solid-body rotation. Fig. 10 shows the convergence of trajectory iteration for the deformation flow. Note that the errors due to spurious divergence decrease rapidly with increasing resolution, and they are negligible compared to those shown in Tables 5 and 8 where the initial conditions are not uniform.

6.3. Solid-body rotation of a cosine bell

For continuous solutions, we test the solid-body rotation of a cosine bell as proposed in [17]. We define the initial condition with the cell-mean values as

$$\bar{\rho}_i = \begin{cases} [1+\cos(\pi r_i/R)]/2, & r_i \leqslant R, \\ 0, & r_i > R, \end{cases} \tag{24}$$

where $R = R_0/3$ is the radius of the cosine bell, and r_i the distance between the ith cell center and the cosine bell center, which is initially placed at $(\lambda, \theta) = (3\pi/2, 0)$. The results are similar for different rotation angles on the geodesic grids, and we present those with $\alpha = \pi/2$ for transport over the poles where the grid is divided into 10 regions.

Table 3 summarizes the errors of the solid-body rotation of the cosine bell with $\alpha = \pi/2$ after one revolution, and Table 4 shows the convergence rates in various resolution intervals. Fig. 11 shows the simulations

Table 2
Statistics of incompressible deformation of a constant field with $\alpha = 0$ after one revolution, using different resolutions and different numbers of trajectory iteration

Grid	Iterations	Minimum	Maximum	ℓ_1 Error	ℓ_2 Error	ℓ_∞ Error
G8	0	0.84137654	1.40067367	0.17739796	0.20447154	0.40067367
G8	2	0.99874870	1.00056522	0.00025555	0.00036390	0.00125130
G16	2	0.99956088	1.00050608	0.00011901	0.00017348	0.00050608
G32	2	0.99979449	1.00020834	0.00004116	0.00006844	0.00020834
G64	2	0.99993794	1.00006051	0.00001073	0.00001899	0.00006206
G128	2	0.99998400	1.00001574	0.00000269	0.00000483	0.00001600

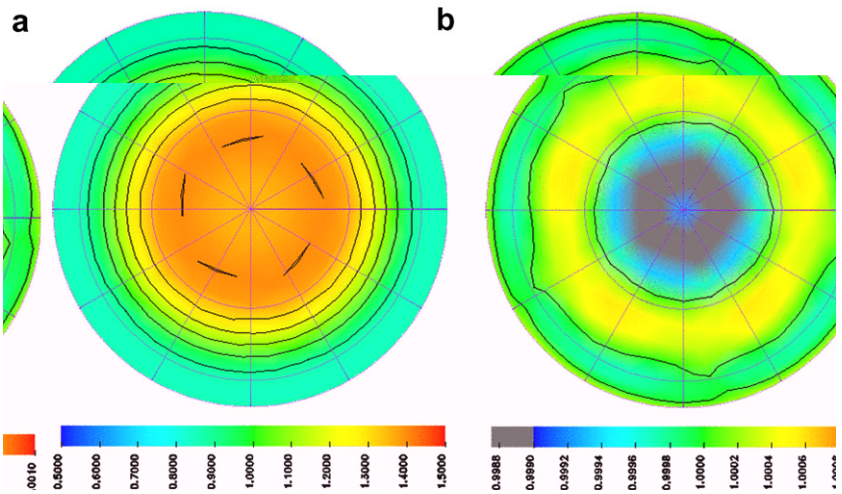

Fig. 10. Incompressible deformation of a constant field with $\alpha = 0$ after one revolution on G8 grid ($\Delta x_e \doteq 1000$ km), using 0 and 2 trajectory iterations in (a) and (b), respectively. The analytic solution has the constant value 1, and the numerical solutions are depicted with both colors and black contours from 0.9 to 1.4 by 0.1. (For interpretation of the references to colour in this figure legend, the reader is referred to the web version of this article.)

Table 3
Statistics of the solid-body rotation of the cosine bell with $\alpha = \pi/2$ after one revolution, using different resolutions (Δx_e)

Grid	Resolution (km)	Minimum	Maximum	ℓ_1 Error	ℓ_2 Error	ℓ_∞ Error
G16	~500	0	0.510	0.555877	0.411567	0.489675
G32	~250	0	0.848	0.117547	0.096496	0.151527
G64	~125	0	0.956	0.019945	0.017232	0.044212
G128	~63	0	0.986	0.003650	0.003829	0.014092

Table 4
Convergence rates of the solid-body rotation of the cosine bell in various resolution intervals

Resolution marching	500 → 250 km	250 → 125 km	125 → 63 km
ℓ_1 Convergence rate	2.24	2.56	2.45
ℓ_2 Convergence rate	2.09	2.49	2.17

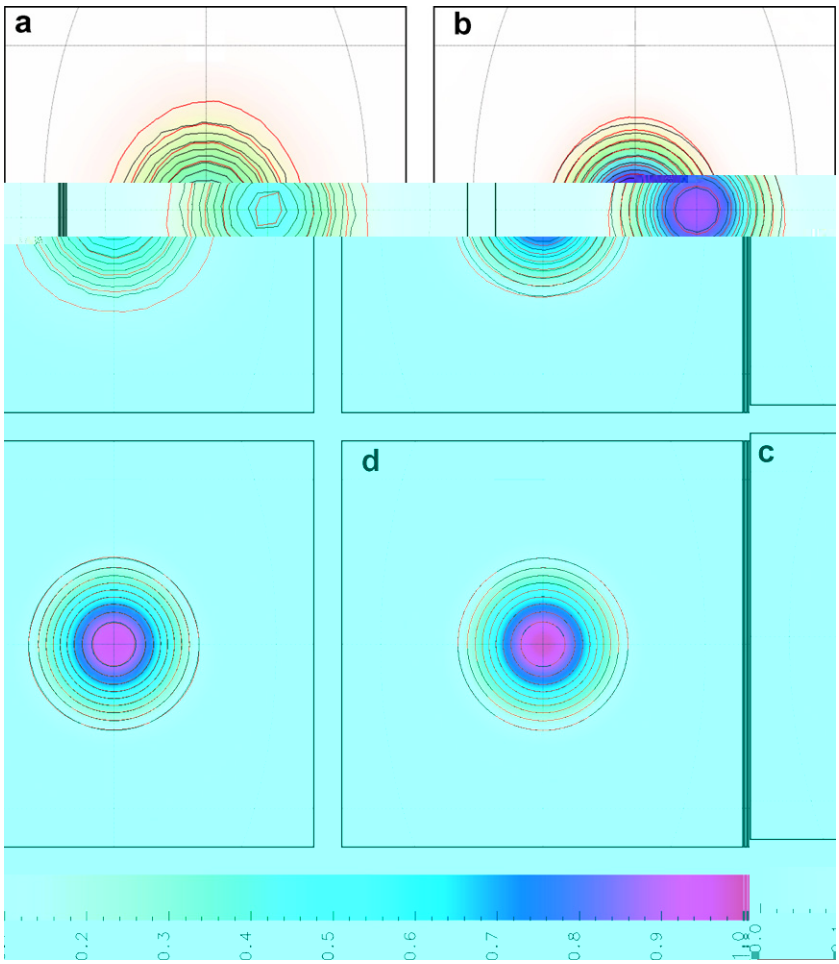

Fig. 11. Solid-body rotation of the cosine bell with $\alpha = \pi/2$ after one revolution at the resolution Δx_e approximately (a) 500 km, (b) 250 km, (c) 125 km and (d) 63 km. The numerical solutions are depicted with both colors and red contours, and the analytic solutions are depicted with black contours from 0.1 to 0.9 by 0.1. (For interpretation of the references to colour in this figure legend, the reader is referred to the web version of this article.)

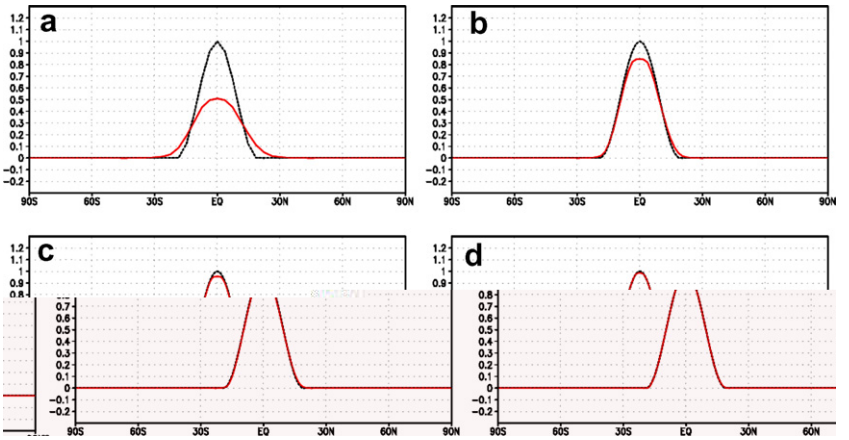

Fig. 12. Profiles of the cosine-bell advection shown in Fig. 11 at $\lambda = 3\pi/2$.

with different resolutions, and Fig. 12 shows the profiles along the meridian at $\lambda = 3\pi/2$, in which direction the cosine bell is transported and the numerical solutions are most deteriorated. We see that the numerical solution converges quickly to the analytic solution with increasing resolution, and the phase speed is almost perfect for all resolutions. The monotonicity is well preserved in all directions, the positive-definiteness is truly achieved, and the shapes of the contours are well maintained with little influence of the grid structure. The amplitudes are, however, not well maintained for low resolutions, because of the low-order spatial accuracy that yields much stronger diffusion for high wave numbers (low resolutions) than for low wave numbers (high resolutions).

Following [11,12], we investigate the convergence of numerical solutions on the geodesic grids in logarithmic scale for each doubling of resolution. For the total error ε in a fixed total integration time, we define the *convergence rate* as $-\Delta \log(\varepsilon)/\log(2)$, which corresponds to the actual order of accuracy in a numerical experiment. We evaluate the convergence rates with the ℓ_1 and ℓ_2 errors but not the ℓ_∞ error, because the ℓ_∞ error is not a mean measure. From Table 4, we observe that the convergence rates of the SSI 2.2 transport scheme are actually greater than its formal spatial order of accuracy (2), because it is also second-order accurate in time. We also note that the convergence of the SSI transport is accelerated at high resolutions, especially with the ℓ_1

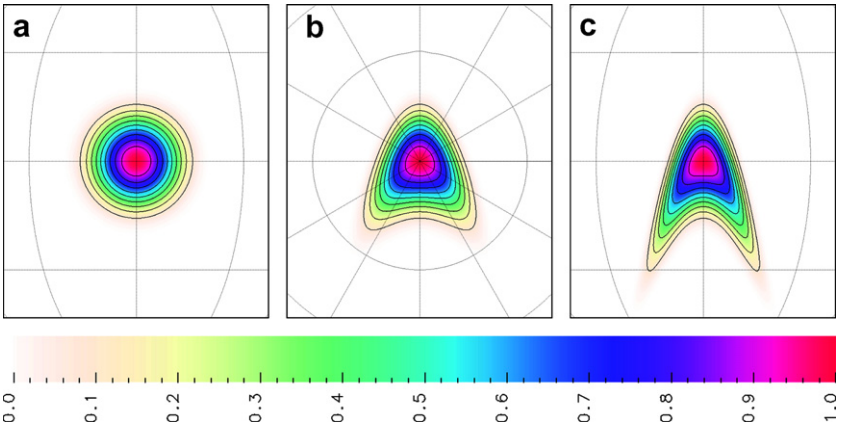

Fig. 13. Analytic solution of the incompressible deformation of the cosine bell with $\alpha = \pi/2$ after (a) 0 or 1 revolution, (b) 1/4 or 3/4 revolution and (c) 1/2 revolution.

measure that is not self-weighted. The fast convergence and the non-linear diffusion indicates that the SSI 2.2 transport is relatively more beneficial for high-resolution applications.

6.4. Incompressible deformation of a cosine bell

For a more realistic experiment, we test the incompressible deformation of the cosine bell. Fig. 13 shows the analytic solution, where the gradients are intensified in the front-left and front-right during the first half revolution, and the cosine bell is resumed during the second half revolution. Although the Lipschitz numbers are very small for high resolutions with the Courant number fixed at 0.5, the total effect of deformation is rather significant.

Table 5 summarizes the errors of the incompressible deformation of the cosine bell with $\alpha = \pi/2$ after one revolution, Table 6 shows the convergence rates in various resolution intervals, and Fig. 14 shows the simulations with different resolutions. The errors of the incompressible deformation are greater than those of the solid-body rotation (Table 3), and the convergence rates of the incompressible deformation are smaller than those of the solid-body rotation (Table 4). These are due to the intensified gradients in the front, and the prolonged distribution in the rear. The intensified gradients increase the wave numbers of the mass distribution with respect to the resolution, causing stronger diffusion from the numerical approximation, and the prolonged distribution enhances the spreading of the errors. The phase speed, the monotonicity, and the positive-definiteness are still well maintained in the deformation flow for all resolutions. The numerical solution has simulated the analytic solution very well at the 63-km resolution, with the convergence continuously accelerated at higher resolutions, confirming that the SSI 2.2 transport scheme is relatively more beneficial for high-resolution applications.

6.5. Solid-body rotation of a cylinder

To better investigate the maintenance of monotonicity and global bounds, we also test the discontinuous solutions with the cylinder as the initial condition:

$$\bar{\rho}_i = \begin{cases} 1, & r_i \leqslant R, \\ 0, & r_i > R, \end{cases} \tag{25}$$

where $R = R_0/3$ is the radius of the cylinder, and r_i the distance between the ith cell center and the cylinder center, which is initially placed at $(\lambda, \theta) = (3\pi/2, 0)$. Because higher resolutions are required for simulating discontinuous solutions, we test the transport of the cylinder with the 125-km and 63-km resolutions only.

Table 5
Statistics of the incompressible deformation of the cosine bell with $\alpha = \pi/2$ after one revolution, using different resolutions (Δx_e)

Grid	Resolution (km)	Minimum	Maximum	ℓ_1 Error	ℓ_2 Error	ℓ_∞ Error
G16	~500	0	0.407	0.801711	0.541144	0.592834
G32	~250	0	0.785	0.324285	0.236165	0.215215
G64	~125	0	0.945	0.093546	0.075869	0.070560
G128	~63	0	0.982	0.020832	0.018013	0.019232

Table 6
Convergence rates of the incompressible deformation of the cosine bell in various resolution intervals

Resolution Marching	500 → 250 km	250 → 125 km	125 → 63 km
ℓ_1 Convergence rate	1.31	1.79	2.17
ℓ_2 Convergence rate	1.20	1.64	2.07

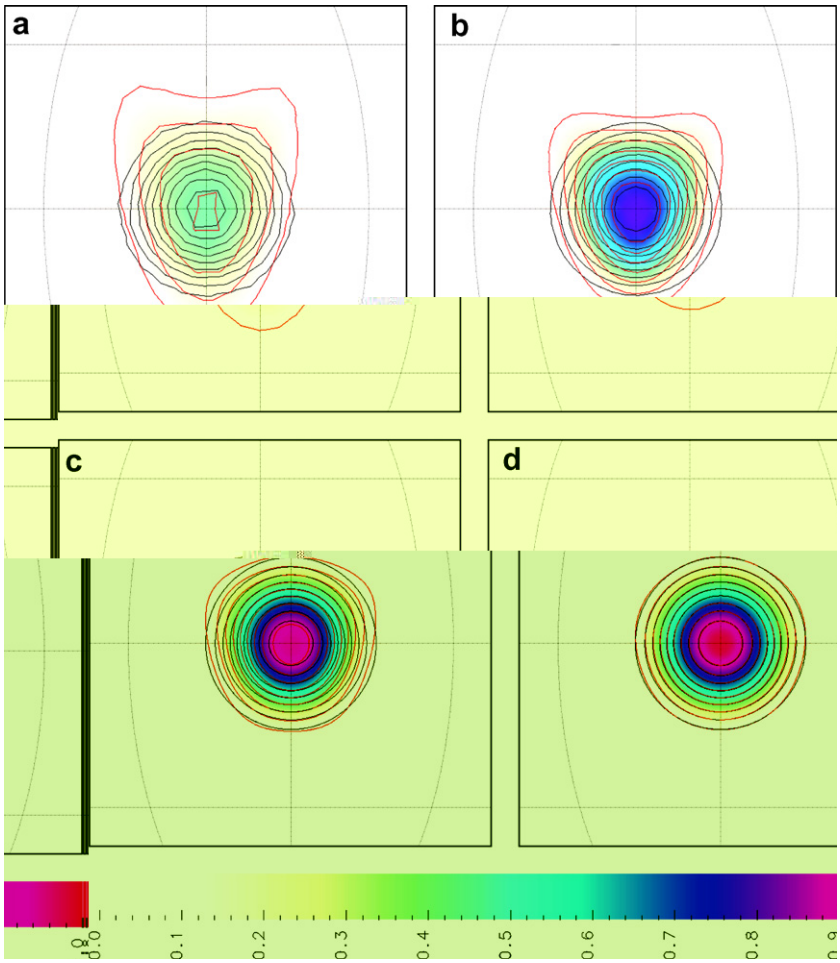

Fig. 14. Incompressible deformation of a cosine bell with $\alpha = \pi/2$ after one revolution at the resolution Δx_e approximately (a) 500 km, (b) 250 km, (c) 125 km and (d) 63 km. The numerical solutions are depicted with both colors and red contours, and the analytic solutions are depicted with black contours from 0.1 to 0.9 by 0.1. (For interpretation of the references to colour in this figure legend, the reader is referred to the web version of this article.)

Table 7
Statistics of the solid-body rotation of the cylinder with $\alpha = \pi/2$ after one revolution, using different resolutions (Δx_e)

Grid	Resolution (km)	Minimum	Maximum	ℓ_1 Error	ℓ_2 Error	ℓ_∞ Error
G64	~125	0	1.0000003	0.190825	0.240614	0.528133
G128	~63	0	1.0000002	0.111653	0.184653	0.530736

Table 7 summarizes the errors of the solid-body rotation of the cylinder with $\alpha = \pi/2$ after one revolution, Fig. 15 shows the simulations with different resolutions, and Fig. 16 shows the profiles along the meridian at $\lambda = 3\pi/2$. The monotonicity and the shape of the discontinuous solutions are maintained as well as those of the continuous ones. The positive-definiteness is firmly achieved by global bounding with local conservation (Section 4), and the overshoots due to the quasi-monotonic constraint are negligible, indicating that the SSI 2.2 is a very good compromise between accuracy and monotonicity. The numerical solution has, however, not yet quite converged to the analytic solution at the 63-km resolution, because the spatial accuracy of the SSI 2.2 transport has reduced to only first-order for maintaining the monotonicity near the sharp gradients.

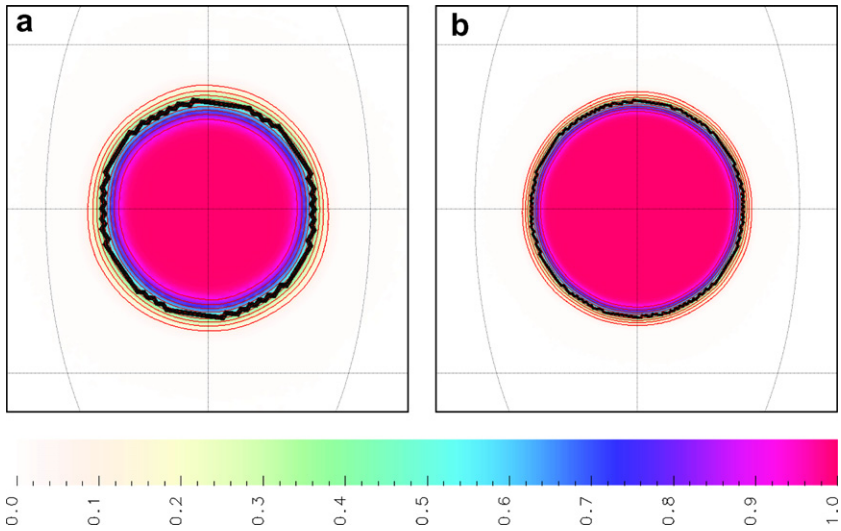

Fig. 15. Solid-body rotation of the cylinder with $\alpha = \pi/2$ after one revolution at the resolution Δx_e approximately (a) 125 km and (b) 63 km. The analytic solutions have the value 1 inside and 0 outside the black circles, and the numerical solutions are depicted with both colors and red contours from 0.1 to 0.9 by 0.1. (For interpretation of the references to colour in this figure legend, the reader is referred to the web version of this article.)

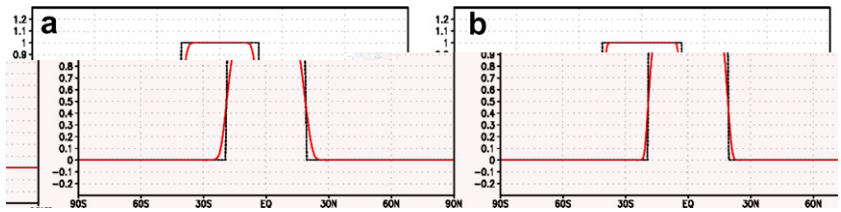

Fig. 16. Profiles of the cylinder advection shown in Fig. 15 at $\lambda = 3\pi/2$.

6.6. Incompressible deformation of a cylinder

To further demonstrate the capability of the SSI method in localizing the errors, we also test the incompressible deformation of the cylinder with $\alpha = \pi/2$. Table 8 summarizes the errors after one revolution, and Fig. 17 shows the simulations with different resolutions. Because the discontinuities cannot be resolved in the discrete grid space, the sharp gradients are quickly diffused. The diffused gradients are, however, strengthened by the deformation flow in the front and weakened in the rear, causing stronger diffusion in the front during the first half revolution. The distortion is thus focused in the front due to the difficulty in resuming the strengthened gradients in the second half revolution. We see that the errors are highly localized, as the solutions in the rear are not contaminated by the greater errors produced in the front. The average phase speed is still very accurate, the monotonicity and the positive-definiteness are still well maintained with negligible overshoots, yet it requires a much higher resolution for the numerical solution to converge to the analytic one.

Table 8
Statistics of the incompressible deformation of the cylinder with $\alpha = \pi/2$ after one revolution, using different resolutions (Δx_e)

Grid	Resolution (km)	Minimum	Maximum	ℓ_1 Error	ℓ_2 Error	ℓ_∞ Error
G64	~125	0	1.000006	0.291320	0.303304	0.711771
G128	~63	0	1.000002	0.168895	0.229042	0.672656

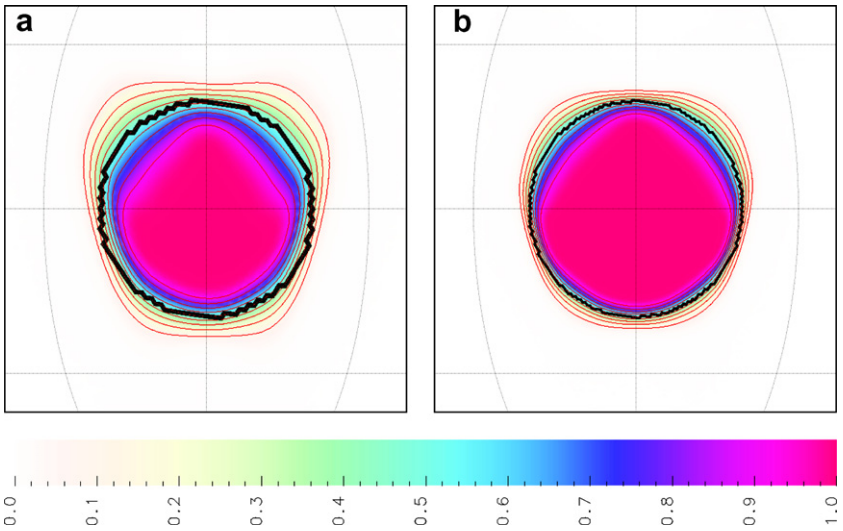

Fig. 17. Incompressible deformation of the cylinder with $\alpha = \pi/2$ after one revolution at the resolution Δx_e approximately (a) 125 km and (b) 63 km. The analytic solutions have the value 1 inside and 0 outside the black circles, and the numerical solutions are depicted with both colors and red contours from 0.1 to 0.9 by 0.1. (For interpretation of the references to colour in this figure legend, the reader is referred to the web version of this article.)

7. Summary and conclusions

A new finite-volume method is proposed for conservative and monotonic transport in multiple dimensions. Lagrangian control volumes are used to trace the invariants in the discrete grid space, and multidimensional subgrid distributions are used to calculate the transport fluxes.

A monotonicity parameter is introduced to optimize the accuracy while maintaining the monotonicity and the global bounds in compressible flows. The monotonicity parameter also provides a means to adjust the amount of diffusion to stabilize the numerical integration. A good variety of quasi-monotonic transport schemes can be conveniently designed for specific purposes by manipulating the monotonicity parameter. We have demonstrated the use of the monotonicity parameter with the SSI 2.2 scheme, which preserves the monotonicity in moderately deformational flows, and guarantees the positive-definiteness in any flows as a lower bound. The SSI 2.2, however, does not constrain the upper bound strictly. Instead, the monotonicity parameter of two is used to optimize the accuracy while providing sufficient diffusion to suppress the overshoots of local maxima to a negligible level. We have found that the numerical solutions converge quickly to the analytic solutions, and the SSI 2.2 is relatively more beneficial for high-resolution applications.

Geodesic grids are used to demonstrate the general geometric nature of the SSI method that the numerical solutions are virtually not affected by the irregularity of grid structure. The SSI method is designed for applications on arbitrary grids, in order to provide the ultimate flexibility for explicit domain decomposition to fully explore the power of modern distributed-memory computers with optimal parallel efficiency. In the beginning phase of the development, we have focused on the application of active transport in a dynamics model that uses explicit time discretizations on quasi-uniform grids for efficient explicit domain decomposition. The time step required by such active transport is much smaller than what is generously allowed by the Lipschitz condition associated with the semi-Lagrangian trajectory iteration. The extension of the SSI method to larger time steps for other applications, such as tracer transport, will be presented in subsequent papers.

Acknowledgments

The reviewers have helped improve the presentation of this article significantly with very constructive comments and suggestions. This work is sponsored by the NASA Earth Science Enterprise through the Global Modeling and Analysis Program.

References

[1] R. Courant, E. Issacson, M. Rees, On the solution of non-linear hyperbolic differential equations by finite differences, Communications on Pure and Applied Mathematics 5 (1952) 243–255.
[2] S.K. Godunov, A difference method for the numerical calculation of discontinuous solutions of hydrodynamic equations, Matematicheskii Sbornick 47 (89) (1959) 271–306, no. 3, Mar;
English Translation: US Department of Commerce, Joint Publications Research Service, no. 7225, November 1960, p. 61.
[3] B. van Leer, Toward the ultimate conservative difference scheme. Part IV: a new approach to numerical convection, J. Comput. Phys. 23 (1977) 276–299.
[4] P. Colella, P.R. Woodward, The piecewise parabolic method (PPM) for gas-dynamical simulations, J. Comput. Phys. 54 (1) (1984) 174–201.
[5] P. Colella, Multidimensional upwind methods for hyperbolic conservation laws, J. Comput. Phys. 87 (1990) 171–200.
[6] S.-J. Lin, R.B. Rood, Multidimensional flux-form semi-Lagrangian transport schemes, Mon. Weather Rev. 124 (9) (1996) 2046–2070.
[7] B. van Leer, Multidimensional explicit difference schemes for hyperbolic conservation laws, Computing Methods in Applied Sciences and Engineering VI, Elsevier Science, New York, 1984, p. 493.
[8] JohnB. Bell, ClintN. Dawson, GregoryR. Shubin, An unsplit, higher order Godunov method for scalar conservation laws in multiple dimensions, J. Comput. Phys. 74 (1988) 1–24.
[9] D.L. Williamson, Integration of the barotropic vorticity equation on a spherical geodesic grid, Tellus 20 (1968) 642–653.
[10] R. Sadourny, A. Arakawa, Y. Mintz, Integration of the non-divergent barotropic vorticity equation with an icosahedral-hexagonal grid for the sphere, Mon. Weather Rev. 96 (1968) 351–356.
[11] R. Heikes, D.A. Randall, Numerical integration of the shallow-water equations on a twisted icosahedral grid. Part I: basic design and results of tests, Mon. Weather Rev. 123 (1995) 1862–1880.
[12] H. Tomita, M. Tsugawa, M. Satoh, K. Goto, Shallow water model on a modified icosahedral geodesic grid by using spring dynamics, J. Comput. Phys. 174 (2) (2001) 579–613.
[13] D.A. Randall, T.D. Ringler, R.P. Heikes, P. Jones, J. Baumgardner, Climate modeling with spherical geodesic grids, Comput. Sci. Eng. 4 (5) (2002) 32–41.
[14] A. Harten, B. Engquist, S. Osher, S.R. Chakravarthy, Uniformly high order accurate essentially non-oscillatory schemes, III, J. Comput. Phys. 71 (1987) 231–303.
[15] A. Robert, A stable numerical integration scheme for the primitive meteorological equations, Atmos. Ocean 19 (1981) 35–46.
[16] A. Staniforth, J. Côté, Semi-Lagrangian interpolation schemes for atmospheric models – a review, Mon. Weather Rev. 119 (1991) 2206–2223.
[17] D.L. Williamson, J.B. Drake, J.J. Hack, R. Jakob, P.N. Swarztrauber, A standard test set for numerical approximations to the shallow water equations in spherical geometry, J. Comput. Phys. 102 (1) (1992) 211–224.
[18] J. Côté, A Lagrange multiplier approach for the metric terms of semi-Lagrangian models on the sphere, Q. J. R. Meteorol. Soc. 114 (1988) 1347–1352.
[19] J. Pudykiewicz, R. Benoit, A. Staniforth, Preliminary results from a partial LRTAP model based on an existing meteorological forecast model, Atmos. Ocean 23 (1985) 267–303.
[20] A. Staniforth, J. Pudykiewicz, Reply to comments on and addenda to "Some properties and comparative performance of the semi-Lagrangian method of Robert in the solution of the advection–diffusion equation", Atmos. Ocean 23 (1985) 195–200.